Proceedings of ALGORITMY 2016
pp. 62–73

IMEX FINITE VOLUME EVOLUTION GALERKIN SCHEME FOR THREE-DIMENSIONAL WEAKLY COMPRESSIBLE FLOWS.*

GEORGIJ BISPEN , MÁRIA LUKÁČOVÁ-MEDVIĎOVÁ , AND LEONID YELASH†

Abstract. In this paper we will derive an implicit-explicit (IMEX) finite volume evolution Galerkin scheme for three-dimensional Euler equations. We will in particular concentrate a singular limit of weakly compressible flows when the Mach number is about $\mathcal{O}(10^{-2}) - \mathcal{O}(10^{-6})$. In order to efficiently resolve slow dynamics we split the whole nonlinear system in a stiff linear part governing the acoustic and gravitational waves and a non-stiff nonlinear part that models nonlinear advection effects. We use stiffly accurate second order IMEX scheme for time discretization to approximate stiff linear operator implicitly and the non-stiff nonlinear operator explicitly. Furthermore in order to take multdimensional effects of flow propagation into account we apply three-dimensional evolution Galerkin operator.

Key words. evolution Galerkin operator, finite volume methods, weakly compressible flows, low Mach number flows, IMEX schemes, asymptotic preserving schemes

AMS subject classifications.

1. Introduction.

This paper presents new implicit-explicit (IMEX) finite volume schemes for three-dimensional weakly compressible flows. In the case of weakly compressible flows the magnitude of flow velocity $\mathbf{u}$ is much slower than the sound speed c, which results in the so-called low Mach number flows. Here the Mach number is a reference number defined as $M = \frac{|\mathbf{u}|}{c}$. Such low Mach number flows arise in many applications, such as meteorology, combustion or astrophysics. We refer also to theoretical works on singular limits of compressible flows, cf. [12, 6]. Development of efficient and stable numerical schemes for weakly compressible flows is a challenging task. In the literature we can find already several studies on this topic. In [1] Bijl and Wesseling have developed a scheme suitable to compute large range of Mach numbers which is based on the finite difference MAC-type scheme for incompressible Euler equations. This approach has been further generalized in [11] and a conservative scheme using the pressure-correction and staggered grid approach (as in the case of the MAC scheme) has been derived and analysed. Another approach, where a numerical scheme for incompressible flows, the so-called SIMPLE method, has been extended to weakly compressible flows has been developed by Munz, Roller, Klein and Geratz in [17]. In this work the formal asymptotic analysis with respect to small Mach number has been used to gain insight into the limit behavior of the compressible flow equations as the Mach number vanishes. Consequently, multiple pressure variables are introduced into the numerical framework, which allowed accurate capturing of various physical phenomena on very different length scales, see also [20] for further developments. Recently, there has been an interesting approach to approximate all Mach numbers flows derived by Feistauer et al. [7, 8], that is based on the higher order discontinuous Galerkin method.

On the other hand, there are techniques that generalize numerical schemes devel-

*This work has been supported by the German Science Foundation under the grants LU 1470/2-3 and TRR 165.

†Institute of Mathematics, Johannes Gutenberg-University Mainz, (bispeng@uni-mainz.de, lukacova@uni-mainz.de, yelash@uni-mainz.de).

oped for compressible flows in order to obtain accurate and stable methods for weakly compressible flows, see, e.g., [13, 10, 5]. Inspired by these works, in our recent work [19] we have split the flux into the stiff/non-stiff parts and applied implicit/explicit time discretization, that yields a nonlinear elliptic equation for the pressure updates. This acts similarly to a classical incompressible projection on the system. Unfortunately the Jacobian of the stiff flux function degenerated in the limit as the Mach number approaches zero and a suitable stabilization was needed. Thus, it implied that the spatial and the temporal grid sizes, Δx and Δt had to be reduced simultaneously as $M \to 0$. Consequently, the resulting scheme has been only *weakly asymptotic preserving*. The concept of the so-called *asymptotic preserving schemes* has been introduced by Jin et al., see [10] and the references therein; a numerical scheme is called asymptotic preserving if it is uniformly consistent as a singular limit parameter, e.g. the Mach number approaches its limit. In particular the scheme reduces to a consistent approximation of the limit equation.

The aim of this paper is to present a new IMEX FV scheme based on the evolution Galerkin (EG) operator in order to approximate multidimensional wave propagation. The EG operator can be considered to be a multidimensional Riemann solver. We refer a reader to our previous works on the finite volume evolution Galerkin methods for the shallow water equations [3] or two-dimensional Euler equations of gas dynamics [16, 15, 14]. As an interesting by-product we will also propose a new IMEX FV scheme that is asymptotic preserving and uniformly accurate as $M \to 0$.

2. Euler equations. Motion of three-dimensional inviscid compressible flows is governed by the Euler equations. They express the basic conservation laws: conservation of mass, momentum and energy. In atmospheric applications it is often more suitable to express the energy equation in terms of potential temperature. We note that for smooth flows both are equivalent. Let $\bar{p}$, $\bar{\rho}$, $\bar{\mathbf{u}}(=0)$, $\bar{\theta}$, $\overline{\rho\theta}$ express the pressure, density, velocity, potential temperature and energy for a background state, which is the hydrostatic equilibrium, i.e.

$$\partial_z \bar{p} = -\bar{\rho} g, \tag{2.1}$$

We will assume that $\bar{\theta} = \text{const}$. Furthermore let $\rho', p', \mathbf{u}', \theta', (\rho\theta)'$ stand for the corresponding perturbations of the background states. Thus, we have $\rho = \bar{\rho} + \rho'$, $p = \bar{p} + p'$, $\theta = \bar{\theta} + \theta'$, and $(\rho\theta) = \overline{\rho\theta} + \bar{\rho}\theta' + \rho'\bar{\theta} + \rho'\theta' \equiv \overline{\rho\theta} + (\rho\theta)'$. Since with the background state $\bar{\mathbf{u}} = 0$, the velocity $\mathbf{u} = \bar{\mathbf{u}} + \mathbf{u}'$ ($\mathbf{u} \in \mathbb{R}^3$) becomes $\mathbf{u} \equiv \mathbf{u}'$, we will omit the prime symbol hereinafter.

In order to avoid numerical instabilities due to the multiscale behaviour of the Euler equations in the case of low Mach number limit the numerical simulations are typically realized for the perturbations, which satisfy the following equations

$$\begin{aligned}
&\partial_t \rho' + \nabla \cdot (\rho \mathbf{u}) = 0 \\
&\partial_t (\rho \mathbf{u}) + \nabla \cdot (\rho \mathbf{u} \otimes \mathbf{u} + p' \,\mathrm{Id}) = -\rho' g \mathbf{e}_3 \equiv -\rho' g \begin{pmatrix} 0 \\ 0 \\ 1 \end{pmatrix} \\
&\partial_t (\rho\theta)' + \nabla \cdot (\rho\theta \mathbf{u}) = 0.
\end{aligned}$$

Denoting T temperature, the potential temperature can be obtained from the equation of adiabatic process in an ideal gas

$$\theta = T \left(\frac{p_0}{p} \right)^{R/c_p}, \; R = c_p - c_v \text{ is the specific gas constant.}$$

In order to close the system we determine pressure from the state equation $p = p_0 \left(\frac{R\rho\theta}{p_0}\right)^\gamma$, where $\gamma = c_p/c_v$ is the adiabatic constant and $p_0 = 10^5 Pa$ the reference pressure. Let us denote by $c = \sqrt{\gamma p/\rho}$ the sound speed, by L the reference length in the vertical direction, by $\varepsilon \equiv M = \frac{|\mathbf{u}|}{c}$ the Mach number and by $Fr = \frac{|\mathbf{u}|}{\sqrt{gL}}$ the Froude number. Rescaling the Euler equation and assuming that $\gamma M^2 = Fr^2$ the Euler equations read

$$
\begin{aligned}
&\partial_t \rho' + \nabla \cdot (\rho \mathbf{u}) = 0 \\
&\partial_t (\rho \mathbf{u}) + \nabla \cdot (\rho \mathbf{u} \otimes \mathbf{u} + \frac{1}{\varepsilon^2} p' \,\mathrm{Id}) = -\frac{1}{\varepsilon^2} \rho' \mathbf{e}_3 \\
&\partial_t (\rho\theta)' + \nabla \cdot (\rho\theta \mathbf{u}) = 0.
\end{aligned} \tag{2.2}
$$

3. Numerical scheme. In order to take into account multiscale behaviour of the solution and to derive an asymptotically stable and accurate scheme, we propose the following splitting of the Euler equations into a linear $\mathcal{L}$ and nonlinear $\mathcal{N}$ part, respectively, see also [16] and the references therein. To this end let us rewrite (2.2) in the following compact form. Let $\mathbf{w} = (\rho', \rho\mathbf{u}, \rho\theta')^T$, $\mathbf{F} = (\rho\mathbf{u}, \rho\mathbf{u} \otimes \mathbf{u} + \frac{1}{\varepsilon^2} p' \,\mathrm{Id}, \rho\theta\mathbf{u})^T$, $S = (0, -\frac{1}{\varepsilon^2}\rho' \mathbf{e}_3, 0)^T$, then (2.2) can be equivalently written as

$$
\frac{\partial \mathbf{w}}{\partial t} = -\nabla \cdot \mathbf{F}(\mathbf{w}) + \mathbf{S}(\mathbf{w}) \equiv \mathcal{L}(\mathbf{w}) + \mathcal{N}(\mathbf{w}). \tag{3.1}
$$

We would like to point out that the choice of the linear and nonlinear operators, $\mathcal{L}$ and $\mathcal{N}$, respectively, is crucial. Indeed we choose $\mathcal{L}$ to model linear acoustic and gravitational waves, whereas the operator $\mathcal{N}$ describes resulting nonlinear advective/convective effects. Analogously as in [16] we set

$$
\mathcal{L}(\mathbf{w}) \equiv -\nabla \cdot \mathcal{F}_L(\mathbf{w}) + S(\mathbf{w}) := -\begin{pmatrix} \nabla \cdot (\rho\mathbf{u}) \\ \frac{1}{\varepsilon^2} \partial p'/\partial x_1 \\ \frac{1}{\varepsilon^2} \partial p'/\partial x_2 \\ \frac{1}{\varepsilon^2} \partial p'/\partial x_3 + \frac{1}{\varepsilon^2}\rho' \\ \nabla \cdot (\bar{\theta}\rho\mathbf{u}) \end{pmatrix} \tag{3.2}
$$

with the linearized pressure $p' = \frac{c_p \bar{p}}{c_v \bar{\rho}\bar{\theta}} (\rho\theta)'$ and

$$
\mathcal{N} \equiv -\nabla \cdot \mathcal{F}_N(\mathbf{w}) := -\nabla \cdot \begin{pmatrix} 0 \\ \rho\mathbf{u} \otimes \mathbf{u} \\ \theta' \rho\mathbf{u} \end{pmatrix}. \tag{3.3}
$$

It is worthwhile to point out that the linear subsystem

$$
\frac{\partial \mathbf{w}}{\partial t} = \mathcal{L}(\mathbf{w}) \tag{3.4}
$$

is stiff having the eigenvalues $\lambda_1 = -\frac{\bar{c}}{\varepsilon}, \lambda_2 = \lambda_3 = \lambda_4 = 0, \lambda_5 = \frac{\bar{c}}{\varepsilon}, \bar{c} = \sqrt{\gamma\bar{p}/\bar{\rho}}$. On the other hand the nonlinear subsystem is non-stiff and its eigenvalues are $\lambda_1 = 0, \lambda_2 = \lambda_3 = \lambda_4 = \mathbf{u} \cdot \mathbf{n}, \lambda_5 = 2\mathbf{u} \cdot \mathbf{n}$, where $\mathbf{n} \in \mathbb{R}^3$ is an arbitrary unit vector.

Consequently, we will discretize the Euler equations by the IMEX scheme in time and approximate the linear stiff system at a new time level t_{n+1} and the nonlinear at the old time level t_n. This yields the first order IMEX scheme. In order to increase

the accuracy the second order IMEX schemes can be applied, see, e.g., [3, 4, 16]. In our recent papers [3, 4] we have studied several second order IMEX schemes with respect to their asymptotic preserving properties. Here we confine ourselves with the second order BDF scheme

$$\mathbf{w}^{n+1} = \alpha_0 \mathbf{w}^n + \alpha_1 \mathbf{w}^{n-1} \\ \beta \mathcal{L}(\mathbf{w}^{n+1}) + \beta_0 \mathcal{N}(\mathbf{w}^n) + \beta_1 \mathcal{N}(\mathbf{w}^{n-1}),$$

$\alpha_0 = \frac{4}{3};\ \alpha_1 = -\frac{1}{3};\ \beta = \frac{2}{3}\Delta t;\ \beta_0 = \frac{4}{3}\Delta t;\ \beta_1 = -\frac{2}{3}\Delta t.$

Spatial discretization is realized by the finite volume scheme. In particular having a regular rectangular grid we approximate the corresponding divergence operators by applying the numerical flux functions in order to approximate fluxes along the cell interfaces. Let us denote the finite difference in the x_1 direction at the mesh cell $\Omega_{i,j,m} \equiv [x_i - \Delta x_1/2, x_i + \Delta x_1/2] \times [y_j - \Delta x_2/2, y_j + \Delta x_2/2] \times [z_m - \Delta x_3/2, z_m + \Delta x_3/2]$ by $\delta_{x_1} f_{i,j,m} \equiv f_{i+1/2,j,m} - f_{i-1/2,j,m}$; an analogous notation holds in the x_2 and x_3 direction. The finite volume discretization of the operators $\mathcal{L}$ and $\mathcal{N}$ yields

$$\mathcal{L}(\mathbf{w}^\ell) = -\sum_{k=1}^{3} \frac{1}{\Delta x_k} \delta_{x_k} \mathcal{F}_L^*(\mathbf{w}^\ell_{i,j,m}) + S(\mathbf{w}^\ell_{i,j,m}), \quad \ell = n+1$$

$$\mathcal{N}(\mathbf{w}^\ell) = -\sum_{k=1}^{3} \frac{1}{\Delta x_k} \delta_{x_k} \mathcal{F}_N^*(\mathbf{w}^\ell_{i,j,m}), \qquad \ell = n, n-1.$$

For the numerical fluxes on cell interfaces, i.e. $\delta_{x_k} \mathcal{F}_L^*(\mathbf{w}^\ell)$ and $\delta_{x_k} \mathcal{F}_N^*(\mathbf{w}^\ell)$, we apply the multidimensional evolution Galerkin operator in the case of linear subsystem and the Rusanov numerical flux for the nonlinear subsystem. For example, the Rusanov flux applied in the x_1-direction gives

$$\mathcal{F}_N^*(\mathbf{w}^\ell_{i+1/2,j,m}) = \frac{1}{2}\left(\mathcal{F}_N(\mathbf{w}^\ell_{i+1,j,m}) + \mathcal{F}_N(\mathbf{w}^\ell_{i,j,m}) - \lambda(\mathbf{w}^\ell_{i+1,j,m} - \mathbf{w}^\ell_{i,j,m})\right) \tag{3.5}$$

with λ denoting the maximum wave speed given by the eigenvalues of (3.3). In the next section we will derive the multidimensional evolution operator EG that predicts the solution on cell interfaces, consequently the multidimensional numerical flux is defined as

$$\mathcal{F}_L^*(\mathbf{w}^\ell_{i+1/2,j,m}) = \frac{1}{\Delta x_2 \Delta x_3} \int_{y_j - \Delta x_2/2}^{y_j + \Delta x_2/2} \int_{z_m - \Delta x_3/2}^{z_m + \Delta x_3/2} \mathcal{F}_L\left(EG(\mathbf{w}^\ell)\right)\Big|_{x_1 = x_{i+1/2}} dz\ dy. \tag{3.6}$$

The second order methods are obtained via MUSCL-type approach using a linear reconstruction in space, we refer a reader to, e.g., [3, 4] for further details. In [4] we have analysed asymptotic preserving properties of the above IMEX FV schemes. In particular, we have shown that the second order IMEX scheme using the BDF scheme in time, the central difference numerical flux for the linear part and the Rusanov numerical flux for the nonlinear one, is asymptotically accurate and stable. For the later any stable numerical flux, e.g. upwind or central fluxes can be chosen, as well.

4. Evolution operator for the linear acoustic subsystem in three space dimensions. In this section we will describe multidimensional evolution operator based on the theory of bicharacteristics for the linear subsytem (3.4). In order to

derive the exact evolution operator we write the linear system (3.4) in a quasilinear form

$$\mathbf{w}_t + \sum_{i=1}^{3} A_i \mathbf{w}_{x_i} = Q, \tag{4.1}$$

with the locally frozen Jacobians

$$A_i = \begin{bmatrix} 0 & \mathbf{e}_i^T & 0 \\ 0 & 0 & \frac{(\bar{c}^a)^2}{\bar{\theta}^a \varepsilon^2}\mathbf{e}_i \\ 0 & \bar{\theta}^a \mathbf{e}_i^T & 0 \end{bmatrix} \tag{4.2}$$

where $\bar{c}^a, \bar{\theta}^a$ denote local averages and the source term

$$Q = -\begin{bmatrix} 0 \\ \frac{1}{\varepsilon^2}(\rho' - (\rho\theta)' \frac{\gamma-1}{\bar{\theta}})\mathbf{e}_3 \\ \rho u_3 \bar{\theta}_{x_3} \end{bmatrix}. \tag{4.3}$$

Let us remark that the source Q contains additional terms due to the product rule applied to $\bar{c}^2/\varepsilon^2\bar{\theta}$ and $\bar{\theta}$.

The system (4.1) is diagonally hyperbolic, i.e. the matrix pencil $P(\mathbf{n}) = \sum_i A_i n_i$ is diagonalizable for any unit vector $\mathbf{n} \in \mathbb{R}^3$, $|\mathbf{n}| = 1$. The corresponding matrices with right and left eigenvectors read

$$R = \begin{bmatrix} \frac{\varepsilon}{\bar{c}^a} & 0 & 0 & 1 & \frac{\varepsilon}{\bar{c}^a} \\ -\mathbf{n} & \mathbf{t}^1 & \mathbf{t}^2 & 0 & \mathbf{n} \\ \frac{\bar{\theta}^a \varepsilon}{\bar{c}^a} & 0 & 0 & 0 & \frac{\bar{\theta}^a \varepsilon}{\bar{c}^a} \end{bmatrix}, \quad R^{-1} = \begin{bmatrix} 0 & 0 & 0 & 1 & 0 \\ -\frac{\mathbf{n}}{2} & \mathbf{t}^1 & \mathbf{t}^2 & 0 & \frac{\mathbf{n}}{2} \\ \frac{\bar{c}^a}{2\bar{\theta}^a \varepsilon} & 0 & 0 & -\frac{1}{\bar{\theta}^a} & \frac{\bar{c}^a}{2\bar{\theta}^a \varepsilon} \end{bmatrix}^T, \tag{4.4}$$

where $\mathbf{n}, \mathbf{t}^1, \mathbf{t}^2$ is an orthonormal basis of $\mathbb{R}^3$. In particular let $\mathbf{n} = \mathbf{n}(\phi, \omega)$, $\phi \in [0, 2\pi), \omega \in [-\pi, \pi]$ be given in spherical coordinates, then we choose $\mathbf{t}^1 = d\mathbf{n}/d\phi$, $\mathbf{t}^2 = d\mathbf{n}/d\omega$ up to multiplicative constants.

$$\mathbf{n} = \begin{bmatrix} \cos(\phi)\sin(\omega) \\ \sin(\phi)\sin(\omega) \\ \cos(\omega) \end{bmatrix}, \quad \mathbf{t}^1 = \begin{bmatrix} -\sin(\phi) \\ \cos(\phi) \\ 0 \end{bmatrix}, \quad \mathbf{t}^2 = \begin{bmatrix} \cos(\phi)\cos(\omega) \\ \sin(\phi)\cos(\omega) \\ -\sin(\omega) \end{bmatrix} \tag{4.5}$$

Multiplying (4.1) by R^{-1} from the left we obtain the system in quasi-diagonal form

$$\mathbf{v}_t + \sum_{i=1}^{3} D_i \mathbf{v}_{x_i} = R^{-1}Q - \sum_{i=1}^{3}(B_i - D_i)\mathbf{v}_{x_i} =: S, \quad \mathbf{v} = R^{-1}\mathbf{w}, \tag{4.6}$$

where $\mathbf{v}$ is the characteristic variable, $B_i = R^{-1}A_i R$ and D_i is the diagonal matrix with the diagonal entries of B_i.

$$\mathbf{v} = \begin{bmatrix} \frac{1}{2}\left[\frac{\bar{c}^a}{\varepsilon\bar{\theta}^a}(\rho\theta)' - \rho\mathbf{u}\cdot\mathbf{n}\right] \\ \rho\mathbf{u}\cdot\mathbf{t}^1 \\ \rho\mathbf{u}\cdot\mathbf{t}^2 \\ \rho' - \frac{(\rho\theta)'}{\bar{\theta}^a} \\ \frac{1}{2}\left[\frac{\bar{c}^a}{\varepsilon\bar{\theta}^a}(\rho\theta)' + \rho\mathbf{u}\cdot\mathbf{n}\right] \end{bmatrix}, \quad B_i = \frac{\bar{c}^a}{\varepsilon}\begin{bmatrix} -n_i & t_i^1 & t_i^2 & 0 & 0 \\ t_i^1 & 0 & 0 & 0 & t_i^1 \\ t_i^2 & 0 & 0 & 0 & t_i^2 \\ 0 & 0 & 0 & 0 & 0 \\ 0 & t_i^1 & t_i^2 & 0 & n_i \end{bmatrix} \tag{4.7}$$

Let us point out that the five families of bicharacteristic curves, $\mathbf{x}^1, ..., \mathbf{x}^5$, of the system (4.1) are given by the ODEs

$$\frac{dx_j^i}{dt} = (D_i)_{jj}, \quad i = 1, ..., 5, \ j = 1, ..., 3. \tag{4.8}$$

For given initial data $\mathbf{x}^i(t^{n+1}) = \mathbf{x}_P$ and arbitrary fixed $\phi \in [0, 2\pi), \omega \in [-\pi, \pi]$ we have

$$\begin{aligned} &\mathbf{x}^1(t;\omega,\phi) = \mathbf{x}_P + (t^{n+1} - t)\bar{c}^a \mathbf{n}(\phi,\omega)/\varepsilon, \quad \mathbf{x}^2(t;\phi,\omega) = ... = \mathbf{x}^4(t;\phi,\omega) = \mathbf{x}_P, \\ &\mathbf{x}^5(t;\phi,\omega) = \mathbf{x}_P - (t^{n+1} - t)\bar{c}^a \mathbf{n}(\phi,\omega)/\varepsilon. \end{aligned} \tag{4.9}$$

Let us consider the quasi-diagonal equation (4.6) along the bicharacteristic curves. Let $\tilde{\mathbf{v}} = (v_1(\mathbf{x}^1, t), ..., v_5(\mathbf{x}^5, t))$, an analogous notation is used for $\tilde{\mathbf{v}}_{x_i}, \tilde{\mathbf{v}}_t, \tilde{Q}$. Realizing that the left-hand side of (4.6) is $d\tilde{\mathbf{v}}/dt$ we have

$$\mathbf{w}(\mathbf{x}_P, t^{n+1}) = R\mathbf{v}(\mathbf{x}_P, t^{n+1}) = R\tilde{\mathbf{v}}(t^n) + \int_{t^n}^{t^{n+1}} R\tilde{S} \ dt, \tag{4.10}$$

where only one bicharacteristic curve for each equation is taking explicitly into account, namely the one determined by the normal vector $\mathbf{n}(\phi, \omega)$. We average along all $\phi \in [0, 2\pi)$, $\omega \in [-\pi, \pi]$ in order to take all infinitely many directions of information propagation into account. Hence, we obtain the genuine multidimensional representation

$$\mathbf{w}(\mathbf{x}_P, t^{n+1}) = \frac{1}{4\pi} \int_0^{2\pi} \int_{-\pi}^{\pi} \left\{ R\tilde{\mathbf{v}}(t^n) + \int_{t^n}^{t^{n+1}} R\tilde{S} \ dt \right\} \sin(\omega) \ d\omega \ d\phi. \tag{4.11}$$

Let us point out that the integrals along the curve $\mathbf{x}^5$ can be rewritten as integrals along $\mathbf{x}^1$, since $\mathbf{x}^5(t;\phi,\omega+\pi) = \mathbf{x}^1(t;\phi,\omega)$. Thus, we can simplify the representation (4.11). Further, the remaining bicharacteristics $\mathbf{x}^2, \mathbf{x}^3, \mathbf{x}^4$ are equal and do not depend on $\mathbf{n}$, i.e. on ϕ and ω. Integrating the continuity and momentum equations in (4.11) along the second bicharacteristic $\mathbf{x}^2$, we obtain that the appearing integrals along the second bicharacteristic can be written in terms of $(\rho\mathbf{u})(\mathbf{x}_P, t^{n+1}), (\rho\mathbf{u})(\mathbf{x}_P, t^n)$. After

some calculations, cf. [2, 3], we obtain the following integral representation

(4.12a)
$$\rho'(\mathbf{x}_P, t^{n+1}) = \left(\rho' - \frac{(\rho\theta)'}{\bar{\theta}^a}\right)(\mathbf{x}_P, t^n) + \frac{(\rho\theta)'}{\bar{\theta}^a}(\mathbf{x}_P, t^{n+1}) + \int_{t^n}^{t^{n+1}} \frac{\rho u_3 \bar{\theta}_{x_3}}{\bar{\theta}^a}(\mathbf{x}_P, t)\ dt$$

(4.12b)
$$\rho u_i(\mathbf{x}_P, t^{n+1}) = -\frac{3\bar{c}^a}{4\pi}\int_0^{2\pi}\int_0^{\pi}\left[\frac{(\rho\theta)'}{\bar{\theta}^a\varepsilon} - \frac{\rho\mathbf{u}\cdot\mathbf{n}(\phi,\omega)}{\bar{c}^a}\right](\mathbf{x}^n, t^n) n_i(\phi,\omega)\sin(\omega)\ d\omega\ d\phi$$
$$- \frac{3\bar{c}^a}{4\pi\varepsilon}\int_{t^n}^{t^{n+1}}\int_0^{2\pi}\int_0^{\pi} f(\mathbf{x}, t, \phi, \omega) n_i(\phi,\omega)\sin(\omega)\ d\omega\ d\phi\ dt$$

(4.12c)
$$(\rho\theta)'(\mathbf{x}_P, t^{n+1}) = \frac{\bar{\theta}^a}{4\pi}\int_0^{2\pi}\int_0^{\pi}\left[\frac{(\rho\theta)'}{\bar{\theta}^a} - \varepsilon\frac{\rho\mathbf{u}\cdot\mathbf{n}(\phi,\omega)}{\bar{c}^a}\right](\mathbf{x}^n, t^n)\sin(\omega)\ d\omega\ d\phi$$
$$+ \frac{\bar{\theta}^a}{4\pi}\int_{t^n}^{t^{n+1}}\int_0^{2\pi}\int_0^{\pi} f(\mathbf{x}, t, \phi, \omega)\sin(\omega)\ d\omega\ d\phi\ dt$$

with $\mathbf{x}^n = \mathbf{x}^1(t^n; \phi, \omega)$ and

(4.12d) $$f(\mathbf{x}, t, \phi, \omega) = -\sum_{j=1}^{2}\mathbf{t}^j\cdot\nabla(\rho\mathbf{u}\cdot\mathbf{t}^j) + \frac{\cos(\omega)}{\bar{c}^a\varepsilon}\left(\rho' - (\gamma-1)\frac{(\rho\theta)'}{\bar{\theta}}\right) - \frac{\rho u_3\bar{\theta}_{x_3}}{\bar{\theta}^a}.$$

Due to its implicit nature we are not able to evaluate the evolution operator (4.12) analytically. To this end we derive an approximate evolution operator by applying the rectangle for time integration over the mantle of the so-called bicharacteristic cone, cf. [14]. Moreover we use the integration by parts[1] in order to rewrite the sum in (4.12d) without the derivatives of $\rho\mathbf{u}$. Hence, we obtain the following approximate

[1]This special integration by parts is referred to as the beautiful or useful lemma in [14].

evolution operator (for the sake of simplicity for smooth data)

(4.13a)
$$\rho'(\mathbf{x}_P,t^{n+1}) = \rho'(\mathbf{x}_P,t^n) - \frac{(\rho\theta)'}{\bar\theta^a}(\mathbf{x}_P,t^n) + \frac{(\rho\theta)'}{\bar\theta^a}(\mathbf{x}_P,t^{n+1}) + \Delta t\frac{\rho u_3\bar\theta_{x_3}}{\bar\theta^a}(\mathbf{x}_P,t^n)$$

(4.13b)
$$\rho u_i(\mathbf{x}_P,t^{n+1}) = -\frac{3\bar c^a}{4\pi}\int_0^{2\pi}\int_0^{\pi}\left[\frac{(\rho\theta)'}{\bar\theta^a\varepsilon} + \frac{\rho u_i}{\bar c^a n_i(\phi,\omega)}\right](\mathbf{x}^n,t^n)n_i(\phi,\omega)\sin(\omega)\ d\omega\ d\phi$$

(4.13c)
$$+\frac{3}{\pi}\int_0^{2\pi}\int_0^{\pi}\rho\mathbf{u}\cdot\mathbf{n}(\phi,\omega)(\mathbf{x}^n,t^n)n_i(\phi,\omega)\sin(\omega)\ d\omega\ d\phi$$
$$-\Delta t\frac{3\bar c^a}{4\pi\varepsilon}\int_0^{2\pi}\int_0^{\pi}h(\mathbf{x},t,\phi,\omega)n_i(\phi,\omega)\sin(\omega)\ d\omega\ d\phi$$

(4.13d)
$$(\rho\theta)'(\mathbf{x}_P,t^{n+1}) = \frac{\bar\theta^a}{4\pi}\int_0^{2\pi}\int_0^{\pi}\left[\frac{(\rho\theta)'}{\bar\theta^a} - 3\varepsilon\frac{\rho\mathbf{u}\cdot\mathbf{n}(\phi,\omega)}{\bar c^a}\right](\mathbf{x}^n,t^n)\sin(\omega)\ d\omega\ d\phi$$
$$+\Delta t\frac{\bar\theta^a}{4\pi}\int_0^{2\pi}\int_0^{\pi}h(\mathbf{x},t,\phi,\omega)\sin(\omega)\ d\omega\ d\phi$$

with $\mathbf{x}^n = \mathbf{x}^1(t^n;\phi,\omega)$ and

(4.13e)
$$h(\mathbf{x},t,\phi,\omega) = \frac{\cos(\omega)}{\bar c^a\varepsilon}\left(\rho' - (\gamma-1)\frac{(\rho\theta)'}{\bar\theta}\right) - \frac{\rho u_3\bar\theta_{x_3}}{\bar\theta^a}.$$

The approximate evolution operator (4.13) is an explicit operator used in time-explicit schemes. In order to obtain the local evolution operator cf. [21, 3, 4, 2] we follow [21], i.e. we consider the limit $\Delta t \to 0$. This can be done rigorously, cf. [4]. However, we want to motivate here that the function f in (4.12) is bounded. Therefore, the time integrals in (4.12) vanish in the limit $\Delta t \to 0$, since $t^{n+1} = t^n + \Delta t$. Consequently, we obtain the local evolution operator

(4.14a)
$$\rho'(\mathbf{x}_P,t^n) = \rho'(\mathbf{x}_P,t^n) - \frac{(\rho\theta)'}{\bar\theta^a}(\mathbf{x}_P,t^n) + \frac{(\rho\theta)'}{\bar\theta^a}(\mathbf{x}_P,t^n)$$

(4.14b)
$$\rho u_i(\mathbf{x}_P,t^n) = -\frac{3\bar c^a}{4\pi}\int_0^{2\pi}\int_0^{\pi}\left[\frac{(\rho\theta)'}{\bar\theta^a\varepsilon} - \frac{\rho\mathbf{u}\cdot\mathbf{n}(\phi,\omega)}{\bar c^a}\right](\mathbf{x}^n,t^n)n_i(\phi,\omega)\sin(\omega)\ d\omega\ d\phi$$

(4.14c)
$$(\rho\theta)'(\mathbf{x}_P,t^{n+1}) = \frac{\bar\theta^a}{4\pi}\int_0^{2\pi}\int_0^{\pi}\left[\frac{(\rho\theta)'}{\bar\theta^a} - \varepsilon\frac{\rho\mathbf{u}\cdot\mathbf{n}(\phi,\omega)}{\bar c^a}\right](\mathbf{x}^n,t^n)\sin(\omega)\ d\omega\ d\phi$$

with $\mathbf{x}^n = \mathbf{x}^1(t^n;\phi,\omega)$ and $\rho'(\mathbf{x}_P,t^n) - \frac{(\rho\theta)'}{\bar\theta^a}(\mathbf{x}_P,t^n)$ are obtained by local averaging of ρ' and $(\rho\theta)'$ at $\mathbf{x}_P$ and time t^n.

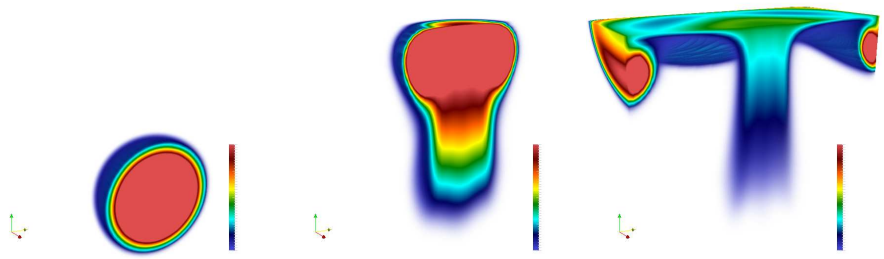

FIG. 1. *Excess potential temperature θ' at times $t = 0$, 500 and 1000s for a rising smooth thermal bubble obtained by the new IMEX finite volume evolution Galerkin schemes. The real-world domain is (1km)^3 (only a half of the computational domain is shown in the x-direction to visualise the interior temperature profiles of the air bubble). Mesh resolution is 64^3 cells; the spatial resolution $1000m/64 = 15.625m$. Colors correspond to values of the potential temperature θ' in range $0 - 0.1K$ and the background color ($\theta' = 0$) has been removed.*

5. Numerical experiment. Using newly developed scheme we conduct a numerical experiment for free convection of a smooth warm air bubble. This test case was first presented by Giraldo and Restelli in [9], see also [18]. We confine ourselves to this test case since it has been computed in [16] using a discontinuous evolution Galerkin scheme which is based on the evolution operator approach, too.

The perturbation of the potential temperature of an air bubble is given by

$$\theta' = \begin{cases} 0 & \text{for} \quad r > r_{\rm c} \\ (\theta'_{\rm c}/2)\,[1 + \cos(\pi r/r_{\rm c})] & \text{for} \quad r \le r_{\rm c}, \end{cases} \tag{5.1}$$

where $\theta'_{\rm c} = 0.5\,{\rm K}$ is the maximal initial amplitude of the perturbation, $r_{\rm c} = 250{\rm m}$ is the bubble radius, and r the distance to the center of the bubble $(x_{\rm c}, y_{\rm c}, z_{\rm c})$. The computation domain is a cube $(1{\rm km})^3$ and the air bubble is placed at $x_{\rm c} = 500{\rm m}$, $y_{\rm c} = 500{\rm m}$, $z_{\rm c} = 350{\rm m}$.

In Figure 1 we present the time evolution of the warm air bubble for $t = 0$, 500 and 1000s. At time $t = 0$ the bubble is resting and spherically shaped, at time $t = 500$s the top of the bubble has just reached the top of the simulation box ($z = 1000$m) and the bubble has deformed to a characteristic symmetric mushroom-like shape due to the shear friction with the surrounding air at the warm/cold air interface. After $t = 500$s the upper part of the air bubble is pressed against the top of the simulation box due to the inertial forces of the advective motion of warm air masses which then slide down along the vertical boundaries of the simulation box, as shown in Figure 1 for time $t = 1000$s. In our simulations we use the no-flux boundary conditions. The mesh resolution in this experiment is 64^3 cells that corresponds to the spatial resolution of $1000{\rm m}/64 = 15.625{\rm m}$ in one dimension.

In order to calculate approximation errors and the order of convergence of the new scheme we needed a reference solution $\mathbf{w}_{\rm ref}$ to compare with a solution $\mathbf{w}_n$ obtained on a mesh with the resolution degree n. An analytical solution for our test experiment is not available but we wish to analyse the convergence of our scheme for a possibly finest mesh. For a desired mesh resolution at least 1024 cells per dimension, a truly 3d-simulation requires a huge amount of computer power to process 10^9 cells. Hence we have decided to generated a set of solutions for up to 1024 cells per dimension in quasi-two dimensional simulations and pickup that one with the finest mesh as a

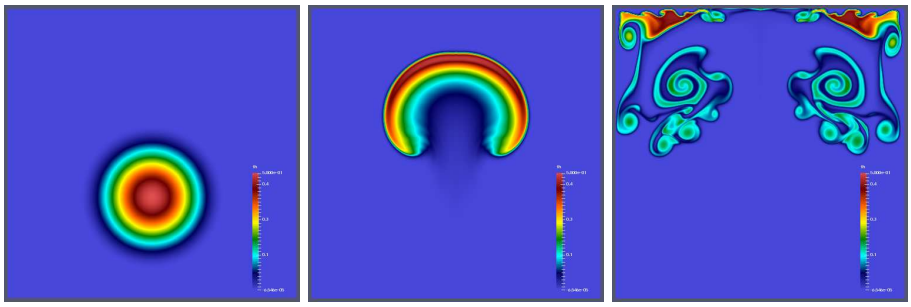

FIG. 2. *Excess potential temperature θ' at times $t = 0$, 500 and 1000s for a rising smooth thermal bubble in quasi-two dimensional simulations obtained by the new IMEX finite volume evolution Galerkin schemes. Mesh resolution $512 \times 1 \times 512$ cells; the spatial resolution $1000m/512 \approx 1.953m$. The real-world domain is $1000m \times 1.953m \times 1000m$.*

reference solution. The quasi-two dimensional means that simulations are performed in a 3d-box in which the y-direction consists of only one layer of cells whereas the x- and the z-directions consist of 2^n cells each. Respectively, the lengths of the box sides were also adjusted to keep the elementary cells cubic shaped. The snapshots of such quasi-2d simulations for $512 \times 1 \times 512$ cells at times $t = 0$, 500 and 1000s are shown in Figure 2. They have been obtained with the same FVEG3D code which we use to generate the 3d results shown in Figure 1.

In Table 1 the experimental order of convergence $EOC(n) = \log_2 \frac{\|\mathbf{w}_n - \mathbf{w}_{\text{ref}}\|}{\|\mathbf{w}_{n+1} - \mathbf{w}_{\text{ref}}\|}$ and the corresponding approximation errors $\|\mathbf{w}_n - \mathbf{w}_{\text{ref}}\|$ in L_1-norms are shown for numerical solutions on a mesh with resolution degree n. One can see that at time $t = 150$s the dominant approximation error is determined by ρu_3, the momentum component in the z-direction, in which the advective motion is being developed due to the buoyancy forces. This variable in the Euler equations determines also the total approximation error and the order of convergence of the whole model (cf. the second and the third columns of Table 1 calculated for the sum of L_1-norms of all variables to those for individual variables). Our numerical experiments clearly demonstrate that the EOC converges to the second order. In this experiment a singular parameter ε was approximately 10^{-2}. In our forthcoming paper [4] we present analysis of asymptotic preserving properties of newly developed IMEX FV schemes for the Euler equations, see also [2].

Acknowledgments. The authors acknowledge the support of the Data Center ZDV in Mainz for providing computation time on MOGON cluster.

REFERENCES

[1] H. BIJL AND P. WESSELING, *A unified method for computing incompressible and compressible flows in boundary-fitted coordinates*, J. Comput. Phys., 141(2) (1998), pp. 153–173.
[2] G. BISPEN, *IMEX finite volume schemes for the shallow water equations*, PhD-thesis, 2015.
[3] G. BISPEN, K. R. ARUN, M. LUKÁČOVÁ-MEDVIĎOVÁ, AND S. NOELLE, *IMEX large time step finite volume methods for low Froude number shallow water flows*, Comm. Comput. Phys., 16 (2014), pp. 307–347.
[4] G. BISPEN AND M. LUKÁČOVÁ-MEDVIĎOVÁ, *Asymptotic preserving IMEX finite volume schemes for low Mach number Euler equations*, in preparation.
[5] P. DEGOND AND M. TANG, *All speed scheme for the low Mach number limit of the isentropic Euler equations*, Commun. Comput. Phys., 10(1) (2011), pp. 1–31.

a) BDF2+EG+MIDPOINT:

	$[\rho', \rho u_1, \rho u_3, (\rho\theta)']$		ρu_3	
n	$\|\mathbf{w}_n - \mathbf{w}_{10}\|$	EOC	$\|\mathbf{w}_n - \mathbf{w}_{10}\|$	EOC
4	4.573e-02	0.8445	1.051e-01	0.8456
5	2.547e-02	1.6043	5.847e-02	1.6625
6	8.376e-03	2.2937	1.847e-02	2.2953
7	1.708e-03	2.5064	3.763e-03	2.5233
8	3.006e-04	2.7175	6.546e-04	2.7328
	ρu_1		θ'	
n	$\|\mathbf{w}_n - \mathbf{w}_{10}\|$	EOC	$\|\mathbf{w}_n - \mathbf{w}_{10}\|$	EOC
4	7.735e-02	0.8426	6.591e-03	0.8122
5	4.313e-02	1.5254	3.754e-03	1.9048
6	1.498e-02	2.2920	1.002e-03	2.9388
7	3.060e-03	2.5006	1.307e-04	3.1213
8	5.406e-04	2.6922	1.502e-05	2.6553

b) BDF2+EG+SIMPSONS:

	$[\rho', \rho u_1, \rho u_3, (\rho\theta)']$		ρu_3	
n	$\|\mathbf{w}_n - \mathbf{w}_9\|$	EOC	$\|\mathbf{w}_n - \mathbf{w}_9\|$	EOC
4	3.565e-02	0.9971	8.030e-02	0.9888
5	1.786e-02	1.9055	4.047e-02	1.9586
6	4.767e-03	2.4213	1.041e-02	2.4091
7	8.900e-04	2.7234	1.960e-03	2.7558
	ρu_1		θ'	
n	$\|\mathbf{w}_n - \mathbf{w}_9\|$	EOC	$\|\mathbf{w}_n - \mathbf{w}_9\|$	EOC
4	6.197e-02	1.0190	4.984e-03	1.1479
5	3.058e-02	1.8267	2.249e-03	2.2635
6	8.622e-03	2.4361	4.684e-04	3.1106
7	1.593e-03	2.6893	5.423e-05	2.7430

TABLE 1

The solution error (L_1-norm) and the experimental order of convergence (EOC) at simulation time $t = 150s$ in the warm air bubble experiment. The spatial integration of the fluxes through the cell boundaries has been performed using (a) the midpoint and (b) the Simpson's rule quadratures.

[6] E. FEIREISL AND A. NOVOTNÝ, *Inviscid incompressible limits of the full Navier-Stokes-Fourier system*, Commun. Math. Phys., 321 (2013), pp. 605–628.

[7] M. FEISTAUER, V. DOLEJŠÍ, AND V. KUČERA, *On the Discontinuous Galerkin Method for the Simulation of Compressible Flow with Wide Range of Mach Numbers*, Computing and Visualization in Science, 10 (2007), pp. 17–27.

[8] M. FEISTAUER, V. KUČERA, *On a robust discontinuous Galerkin technique for the solution of compressible flow*, J. Comput. Phys., 224 (2007), pp. 208–221.

[9] F.X. GIRALDO, AND M. RESTELLI, *A Study of Spectral Element and Discontinuous Galerkin Methods for the Navier-Stokes Equations in Nonhydrostatic Mesoscale Atmospheric Modeling: Equation Sets and Test Cases*, J. Comput. Phys., 227 (2008), pp. 3849–3877.

[10] J. HAACK, S. JIN, AND J.-G. LIU, *An all-speed asymptotic-preserving method for the isentropic Euler and Navier-Stokes equations*, Commun. Comput. Phys., 12 (2012), pp. 955–980.

[11] D.R. VAN DER HEUL, C. VIUK, AND P. WESSELING, *A conservative pressure-correction method for flow at all speeds* Computers & Fluids, 32(8) (2003), pp. 1113–1132.

[12] S. KLAINERMAN AND A. MAJDA, *Singular limits of quasilinear hyperbolic systems with large parameters and the incompressible limit of compressible fluids*, Comm. Pure Appl. Math., 34(4) (1981), pp. 481–524.

[13] R. KLEIN, *Semi-implicit extension of a Godunov-type scheme based on low Mach number asymptotics I. One-dimensional flow*, J. Comput. Phys., 121(2) (1995), pp. 213–237.

[14] M. Lukáčová-Medviďová, and K.W. Morton, *Finite volume evolution Galerkin methodsa survey*, Indian J. Pure Appl. Math., 41 (2010), pp. 329–361.
[15] M. Lukáčová-Medviďová, K.W. Morton, and G. Warnecke, *Finite volume evolution Galerkin methods for hyperbolic systems*, J. Sci. Comput., 26(1) (2004), pp. 1–30.
[16] M. Lukáčová Medviďová, A. Müller, V. Wirth, and L. Yelash, *Adaptive discontinuous evolution Galerkin method for dry atmospheric flow.* J. Comput. Phys., 268 (2014), pp. 106–133.
[17] C.-D. Munz, S. Roller, R. Klein, K.J. Geratz, *The extension of incompressible flow solvers to the weakly compressible regime* Computers & Fluids, 32(2) (2003), pp. 173–196.
[18] A. Müller, J. Behrens, F.X., Giraldo, and V. Wirth, *Comparison between adaptive and uniform discontinuous Galerkin simulations in dry 2D bubble experiments*, J. Comput. Phys., 235 (2013), pp. 371–393.
[19] S. Noelle, G. Bispen, K.R. Arun, M. Lukáčová-Medviďová, C.-D. Munz, *A weakly asymptotic preserving low Mach number scheme for the Euler equations of gas dynamics*, SIAM J. Sci. Comput., 36(6) (2014), pp. 989–1024.
[20] J. H. Park and C.-D. Munz, *Multiple pressure variables methods for fluid flow at all Mach numbers*, Internat. J. Numer. Methods Fluids, 49(8) (2005), pp. 905–931.
[21] Y. Sun, and Y.-X. Ren, *The finite volume local evolution Galerkin method for solving the hyperbolic conservation laws*, J. Comput. Phys., 228(13) (2009), pp. 4945–4960.